Quantitative Analysis of an Airblast Atomizer in the Near-field Region Using Broadband and Narrowband X-ray Measurements

D. Li[1*], J. K. Bothell[1], T. B. Morgan[1], T. J. Heindel[1],
A. Aliseda[2], N. Machicoane[2], A. L. Kastengren[3]
[1]Department of Mechanical Engineering, Iowa State University, USA
[2]Department of Mechanical Engineering, University of Washington, USA
[3]Advanced Photon Source, Argonne National Laboratory, USA

Abstract

Airblast atomizers are widely used in many industries including fuel combustion, atomization drying, and spray painting. The quality of the spray, however, has a large impact on the efficiency and effectiveness of the spray process. Understanding the primary breakup mechanism(s) in the near-field region of the spray is critical if one wants to control it to provide better spray characteristics. Traditional optical imaging methods in this region are extremely challenging because the near-field region is generally optically dense. In contrast, X-ray imaging can penetrate the near-field region and provide quantitative measurements to enhance our knowledge of this spray region.

In this study, a broadband and narrowband X-ray source were used in the near-field region of a canonical coaxial airblast atomizer. To enhance image contrast with the broadband source, 20% potassium iodide was added to the liquid phase. The narrowband X-ray source was used to determine the equivalent path length because the X-ray absorption coefficient is known exactly for the given monochromatic X-ray beam. These measurements were compared to a calibrated broadband source where a penumbra and beam hardening/ attenuation coefficient correction were needed to provide accurate results.

Keywords: Airblast atomizer, narrowband X-ray, broadband X-ray, radiography

Introduction

Sprays are used in a wide range of industrial applications, including spray-dying in chemical engineering [1], fuel combustion in aircraft engines [2], painting in manufacturing processes [3], etc. The spread of the spray and the size of spray droplets are closely related to the efficiency of the process. Most sprays can be divided into a near-field region and a far-field region. The near-field region covers the dense spray near the nozzle exit, where primary breakup processes and injector flow dynamics are critical factors that influence the formation of the spray [4].

The near-field region is generally optical dense and visualizing the spray in this region is challenging. Ballistic imaging [5] and structured laser illumination imaging [6] are examples of laser-based imaging techniques that have been used in the near-field region. However, the measurements could be inaccurate due to the absorption, reflection, and multiple scattering events caused by the large number of gas-liquid interfaces from the atomization process [7]. Alternatively, X-ray imaging can be used to probe the inner structure of the spray owing to the weak scatter and penetrating nature of X-rays.

X-ray radiography is the act of using X-rays to obtain a shadow-like image of an object where the brightness and darkness of the "shadow" are a function of X-ray power and attenuation [8]. Several research groups have used this technique to study sprays, as is done at the Advanced Photon Source (APS) at Argonne National Laboratory [9-11]. The APS provides high-resolution high-flux X-ray beams for various scientific and technological studies. The white beam X-ray from APS provides a broadband, temporally resolved image of a sub region of a spray. Because the beam is limited in size, white beam X-ray imaging at APS cannot provide a single image of the entire spray. This technique can be used to capture high-speed video [12] and details of liquid breakup [13]. The APS also provides a monochromatic X-ray beam, which provides highly time-resolved point measurements. A very narrow pencil-beam of nearly monochromatic X-rays are passed through the spray at a certain point from which the equivalent path length (EPL) of the spray at that location can be determined at the given instant in time. The APS narrowband X-ray source can provide more accurate EPL measurements because a monochromatic X-ray source eliminates beam hardening effects that can influence broadband measurements [14]. One limitation of narrowband X-rays at APS is that only discrete data points can be acquired in a raster-scan process when taking data to cover the entire spray. The APS provides accurate and detailed data, but it has a limited field of view as well as limited access.

[*] Corresponding author, danyuli@iastate.edu

The Experimental Multiphase Flow Laboratory at Iowa State University (ISU) houses two broadband X-ray tube sources, which are easier to operate and more flexible than the APS X-ray source. X-rays are produced by cathode ray tubes, and they hit an anode to produce X-rays. Different in formation, the broadband X-ray tube source at ISU produces an X-ray cone beam that provides a much larger field of view compared to APS. It provides a time-averaged resolution for the full view of the spray all at once. Compared to the APS synchrotron X-ray source, the broadband X-ray source at ISU has lower spatial and temporal resolution but is more economical to operate and covers a much larger field of view. An initial comparison between these two sources was completed by Halls et al. [15] using an impinging jet spray.

The goal of this paper is to compare the ISU X-ray imaging facility to the APS facility using data from the near-field region of an airblast atomizer. This paper compares time-averaged equivalent path length measurements from the two sources at various axial locations from the exit of the airblast atomizer. Fixed liquid and gas flow rates were investigated at three different swirl ratios (SR = 0, 0.5, 1), which is the ratio of swirl air to co-flow air. For the broadband X-ray source at ISU, the penumbra effect caused by a finite size X-ray source is shown to affect the measurement and corrections have been applied.

Experimental Setup

Figure 1 is a schematic of the experimental facility at ISU. X-rays are produced in a lead-lined X-ray vault, and the airblast atomizer is mounted inside this facility. The aluminium airblast atomizer is identical to the one used by the University of Washington [16], but is mounted vertically with the spray pointing down. A polyimide sheet, which is transparent to X-rays, surrounded the spray to protect the equipment. A large-diameter funnel connects to a wet-vacuum provides a slight suction at the spray exit to collect any droplets and prevent recirculation. The captured fluid is returned to the water tank for reuse. The flow meters, flow controllers, and the liquid tank are located outside the X-ray vault. Constant velocity liquid is forced from the holding tank using high pressure air, and the liquid is injected from both sides of a liquid plenum to create a liquid jet at the center of the airblast atomizer. Air is first divided into co-flow air (entering perpendicular to the liquid jet axis) and swirl air (entering tangent to the liquid jet axis), and each of the air streams is then branched into four streams to enter the airblast atomizer from four orthogonal directions. Electronic proportioning valves are used on the air stream line to control the total air flow rates exactly. The experimental setup at APS is identical, with the exception that (1) a different X-ray source is used, (2) a different system is used to measure X-ray intensity, (3) no polyimide sheets are used, and (4) the exhaust system is reduced in size buy operated in a similar fashion.

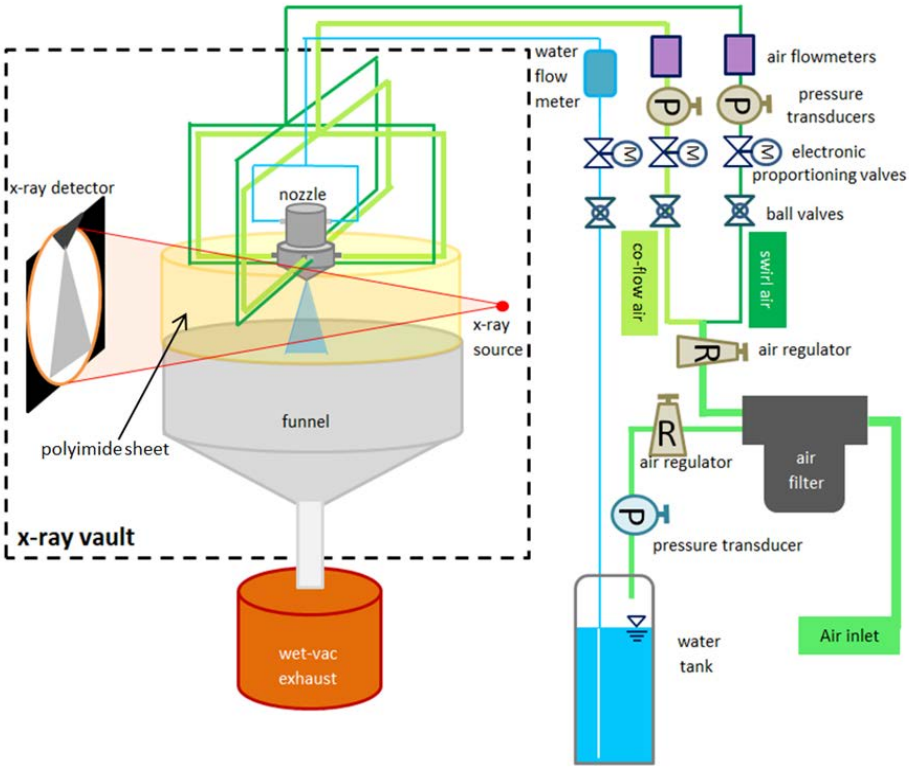

Figure 1: The airblast atomizer flow loop at Iowa State University.

The broadband X-ray imaging facility at ISU [17] contains two LORAD LPX200 portable sealed tube sources that are positioned ninety degrees from each other, and each produce an X-ray cone beam. Either an

image intensifier or a cesium-iodide phosphor screen can be used to convert the X-ray intensity to visible light. The two sources can be used together to take stereographic images or used individually to take radiographic or computed tomographic images. Here only one X-ray source was used to take radiographs, because of the symmetric feature of the spray. The voltage of the X-ray source can be varied from 10 to 200 keV and influences X-ray penetration. The current of the X-ray source can range from 0.1 to 10.0 mA and influences image contrast. In this study, 50 keV voltage and 2.0 mA current were used. Pictures of the fluorescing cesium-iodide phosphor screen were acquired with an Apogee Alta U9 camera with a 50 mm, f/1.2 lens and stored as 16-bit images. In this research, radiographs were taken at 10 frames per second for 2 minutes (1200 frames) at each condition, with an image size of approximately 117 mm x 86 mm (1388 x 1024 pixels). The exposure time was 20 ms.

The 7-BM beamline at APS was used in this research to acquire narrowband X-ray time-resolved radiography [9]. A water-cooled double-multilayer monochromator was used to create the monochromatic beam. The energy range of 8 keV mean photon energy, 4% ΔE/E bandpass, and 5 x 7 μm full width at half maximum beam focus size. A PIN diode was used to record the X-ray intensity of the focused beam X-ray using techniques similar to Kastengren et al. [9-11].

The image processing was based on the Beer-Lambert law: If a monochromatic X-ray beam with intensity of I_o traverses through a medium, the X-ray energy will be attenuated to I because of absorption [18]. If the medium is a single phase homogenous material, the relationship between I and I_o is shown as:

$$\ell = I_o \exp(\mu \cdot \ell) \tag{1}$$

where μ is the attenuation coefficient and ℓ is the X-ray path length through the medium. I_o and I can be obtained from the radiographic images in regions without and with the spray, respectively. For the narrowband X-ray source at APS, the attenuation coefficient can be regarded as constant and known. For the broadband X-ray tube source at ISU, μ is not a constant due to beam hardening and the broad energy spectrum that produces the X-rays. For a spray, the discontinuous liquid phase is distributed in a continuous gas phase. Air is approximately transparent to X-rays. So all X-ray absorption occurs in the discontinuous liquid phase, and the path length is replaced by the equivalent path length (EPL) of the liquid phase. The product of μ and ℓ is a dimensionless parameter called the optical depth (OD).

In this research, air and water were mixed at the nozzle exit to create a spray. The inner and outer diameter of the liquid nozzle was 2.1 mm and 2.7 mm, respectively, and the inner diameter of the air outlet was 10.0 mm. The liquid Reynolds number (Re_l) was defined as:

$$Re_l = (U_l \cdot D_i)/\nu_l \tag{2}$$

where U_l is the mean liquid velocity at the nozzle exit (it was 0.48 m/s in this study), D_i is the inner diameter of the liquid nozzle, and ν_l is the kinematic viscosity of water. The Re_l in this experiment was 1,000 with a liquid flow rate of 0.099 liters per minute.

The gas liquid Reynolds number (Re_g) was defined as:

$$Re_g = (U_g \cdot D_h)/\nu_g \tag{3}$$

where U_g is the mean air velocity at the nozzle exit, D_h is the air hydraulic diameter at the nozzle exit, and ν_g is the kinematic viscosity of air. For the concentric nozzle configuration D_h is defined by the difference between the inner diameter of the air outlet and the outer diameter of the liquid nozzle. In this study, the Re_g was 16,700 with an air flow rate of 150 standard liters per minute.

As mentioned above, air was divided into co-flow air and swirl air. Co-flow air stretched and broke the liquid phase in the axial direction, while the swirl air sheared the liquid in the azimuthal direction. The swirl ratio (SR) was defined as the ratio between the flow rate of the swirl air compared to the co-flow air, as shown in equation (4). Three swirl ratios (SR = 0, 0.5, and 1) were investigated in this study. Note that the total air flow rate remained constant as the swirl ratio varied.

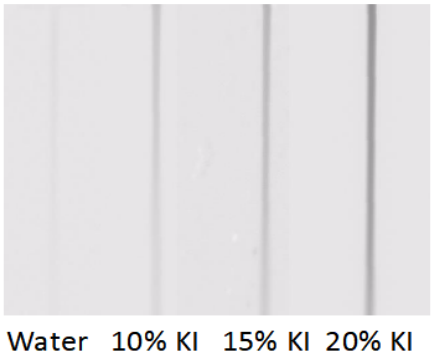

Figure 2: Radiographs of a liquid stream with changing KI

SR = (swirl air flow rate) / (co-flow air flow rate) (4)

At APS, distilled water was used as the liquid phase. At ISU, the contrast between water and air was not sufficient and did not produce a sufficient signal-to-noise ratio. To enhance contrast, 20% potassium iodide (KI) by mass was added in the water. Figure 2 shows radiographs of a liquid stream emanating from the 2.1 mm inner diameter liquid nozzle at differing KI concentrations. It has been shown that KI concentration has a linear relationship with the X-ray attenuation coefficient with KI concentrations as high as 20% [15]. Hence, the 20% KI will not significantly enhance beam hardening.

Data processing

The penumbra effect [19] may influence the radiographic imaging at ISU. This happens when the X-ray source cannot be considered a point source and is magnified as the distance from the object to the detector is increased. The X-ray tube source at ISU has an effective spot size of 1 mm (a 1 mm sq. beryllium window after the 1.5 mm diameter focus spot), as shown in Figure 3. Hall et al. [15, 20] decreased the distance between the detector and the spray to minimize the penumbra effect. In this research, the distance between the source and the spray center was 1290 mm, while the distance between the detector and the spray center was 590 mm. Due to physical limitations of the funnel catch system and the polyimide sheet, the spray-detector distance could not be shortened and the penumbra effect had to be considered.

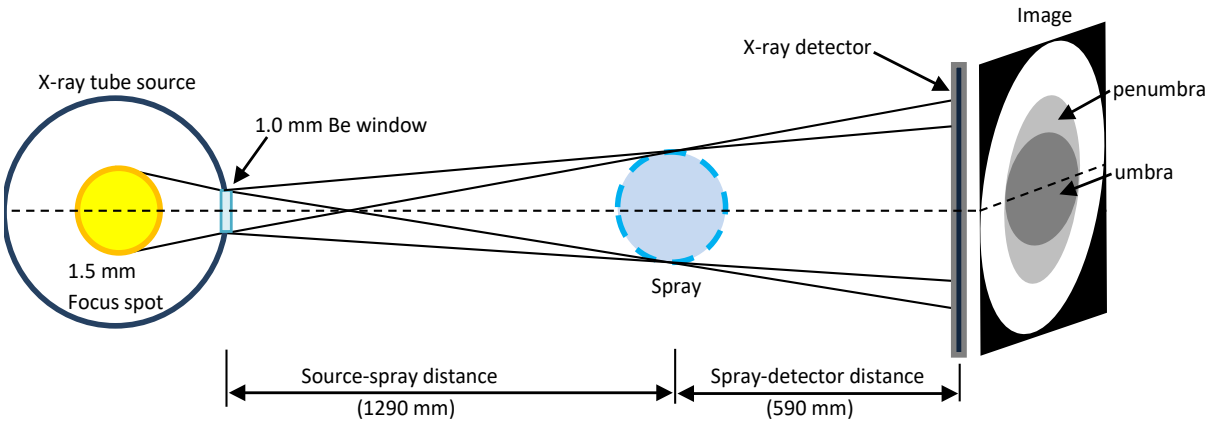

Figure 3: The penumbra effect in the ISU X-ray facility (not to scale).

The penumbra effect is more obvious at the edges than in the center, causing EPL distribution errors. The theoretical evaluation of the penumbra effect on the EPL distribution of a liquid stream is shown in Figure 4. The blue line shows the EPL distribution along the horizontal direction of a liquid stream, with an ideal point X-ray source assumption. The diameter of the liquid stream was 2 mm, and it was magnified to approximately 2.9 mm at the detector by the cone beam as shown by the blue line. The red dash line shows a theoretical computation of the EPL distribution considering the size of the X-ray source spot size and accounting for the penumbra effect. The penumbra effect is uneven, with the primary influence near the edges of the liquid stream where the image is stretched in the horizontal direction from approximately 2.9 mm in diameter to approximately 3.6 mm in diameter. To match the narrowband results at APS, a shape correction is needed for the ISU broadband source. The two curves in Figure 4 were used to determine the penumbra effect calibration as shown in Figure 5. This correction was more significant at low EPL. Research continues to improve the calibration.

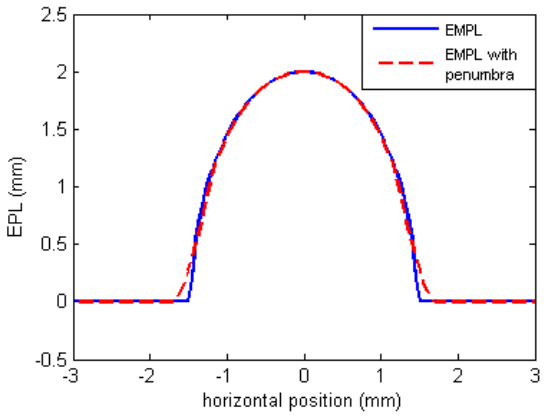

Figure 4: The penumbra effect on a 2 mm diameter liquid stream.

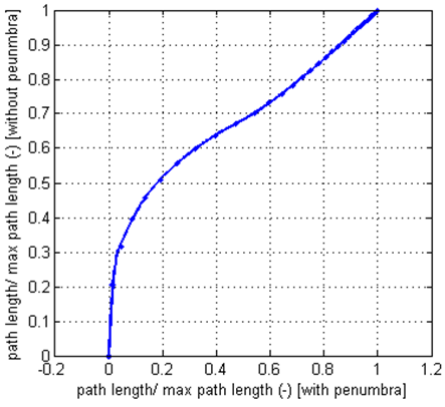

Figure 5: Penumbra effect calibration curve.

In addition to the penumbra effect, beam hardening and the complex attenuation coefficeint caused by the broad energy spectrum of the ISU tube source, must also be accounted for. Using the exact same airblast atomizer and flow conditions, a beam hardening/ attenuation coefficient calibration was developed using data from the narrowband APS and broadband ISU measurements. In both cases, the center part of the spray was unaffected by the penumbra effect and the EPL from APS can be used to correct the ISU broadband data. Hence from Equation (1):

$$(OD)_{ISU} / \mu_{ISU} = EPL_{ISU} = EPL_{APS} = (OD)_{APS} / \mu_{APS} \quad (5)$$

where μ_{APS} is the known absorption coefficient for the given narrowband beam wavelength. Figure 6 shows the relationship between the narrowband APS and broadband ISU measurements, for the same spray. The gradient of the curve is the effective attenuation coefficient, μ_{ISU}, which is a function of liquid thickness due to beam hardening effects and wavelength from the broad energy spectrum of the broadband tube source. This curve was used to calibrate the effect of beam hardening/ attenuation coefficient.

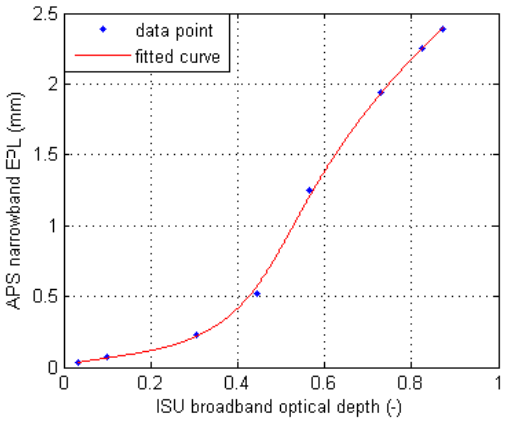

Figure 6: Beam hardening calibration curve relating optical depth to effective mean path length.

Results and Discussion

Figure 7 shows the optical depths at position y = 1 mm below the nozzle exit and SR = 0, both from broadband and narrowband X-rays. The red circles represent APS narrowband X-ray data points, and the blue crosses represent ISU broadband data points. According to Equation (5), the difference in attenuation coefficient leads to the differing measures of optical depth at the same axial position. Therefore, EPL is employed as a consist measurement to quantify the spray.

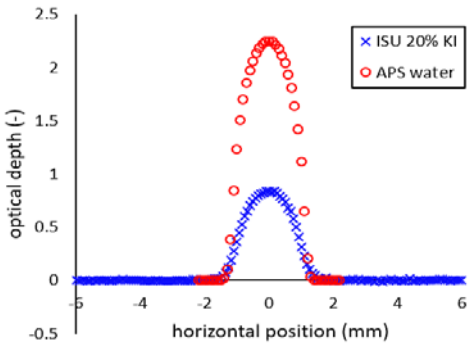

Figure 7: Optical depth distribution at y = 1 mm below the nozzle, and SR = 0.

Figures 8 to 13 show the EPL of the spray at various positions, with different swirl ratios. The "BH" in the legend means only the beam hardening/ attenuation coefficient calibration was applied to the data, and the "BH+P" means that both beam hardening/ attenuation coefficient and penumbra effect calibrations were applied.

Figure 8 shows the EPL with SR = 0 at a position close to the nozzle exit (y = 1 mm below the nozzle tip). The APS narrowband EPL (shown in red circles) are employed as true data. More details about the APS narrowband data can be found in a companion paper [21]. The black crosses represent the ISU broadband data points with only the beam hardening/ attenuation coefficient calibration. The blue dots represent the ISU broadband data points with both beam hardening/ attenuation coefficient and penumbra effect calibration. To compare with the APS data, the ISU data in Figures 8 to 13 have been corrected for the cone beam magnification to show the real size of the spray. According to Figure 8, the maximum EPL at the center is 2.2 mm and all data processing methods in this region show similar results. The penumbra effect calibration seems to work well when the EPL is larger than 0.4 mm. When the EPL is small, the calibrated value is larger than it should be, which causes the horizontal range of the spray to be stretched from 2.8 mm to 3.6 mm, causing a 43% error. Moreover, the penumbra effect calibration also amplifies noise at small EPL as shown in the tails of the ISU data.

Figure 9 shows the EPL at a lower positions (y = 7 mm below the nozzle tip) at the same flow condition as that of Figure 8 (SR = 0). The width of the spray is around 5.4 mm. According to the APS data, the maximum EPL is 0.28 mm, while that of ISU data is about 0.23 mm, 18% smaller. The beam hardening/ attenuation coefficient calibration is not as accurate at this small EPL. Since the overall EPL is small, the penumbra effect calibration starts to lose efficacy and enhance noise. The noise amplitude of the ISU EPL with two calibrations is magnified to ~0.08 mm.

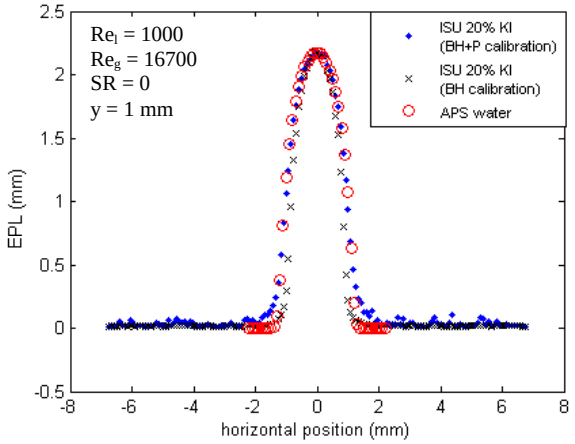

Figure 8: EPL at y = 1 mm below the nozzle, and SR = 0.

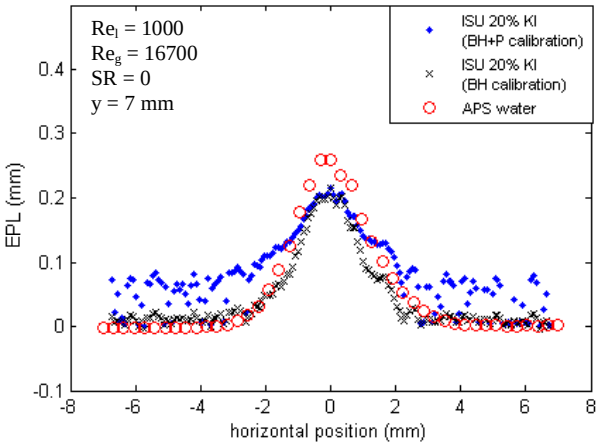

Figure 9: EPL at y = 7 mm below the nozzle, and SR = 0.

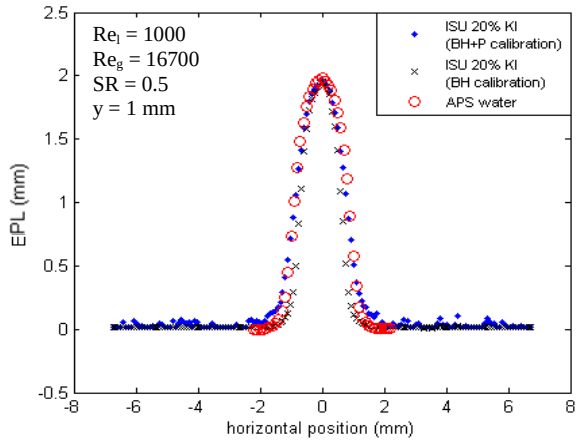

Figure 10: EPL at y = 1 mm below the nozzle, and SR = 0.5.

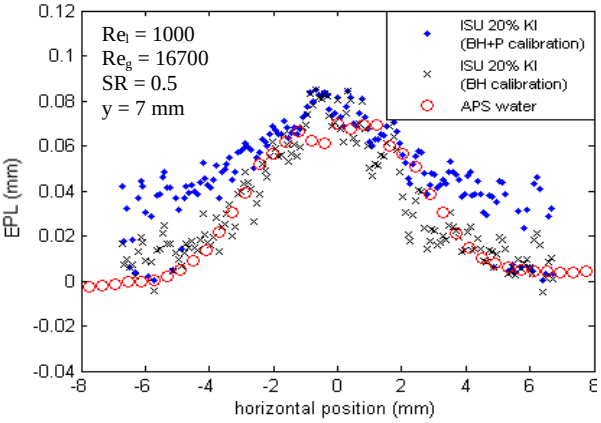

Figure 11: EPL at y = 7 mm below the nozzle, and SR = 0.5.

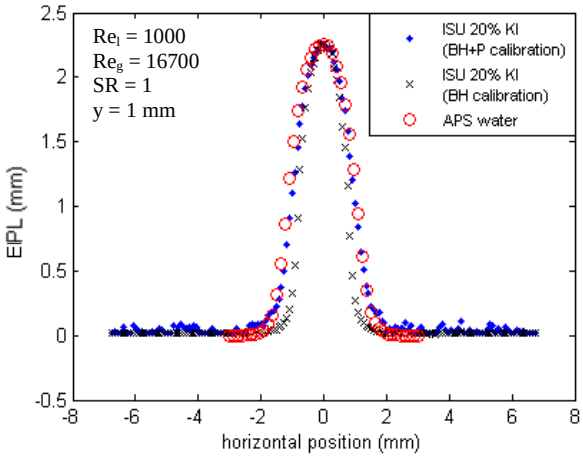

Figure 12: EPL at y = 1 mm below the nozzle, and SR = 1.

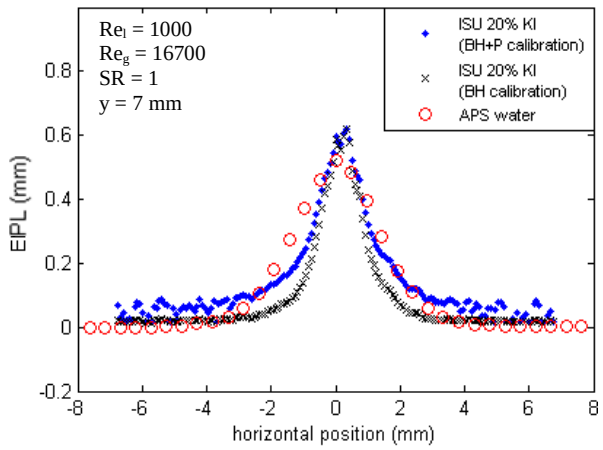

Figure 13: EPL at y = 7 mm below the nozzle, and SR = 1.

The EPL distributions at swirl ratios equal to 0.5 and 1 are shown in Figures 10 to 13. In general, at the position close to the nozzle, the penumbra correction works well (Figures 8, 10 and 12), especially at the center part where the penumbra corrected results achieve high conformity to the APS narrowband data. However, at

the spray edges, the penumbra corrected ISU broadband EPLs are slightly larger than the APS data. At positions farther from the nozzle exit where the spray spreads out, the penumbra effect calibration does not work as well as Figures 9, 11 and 13 suggest, but here the overall EPL is also much smaller. The penumbra effect calibration performs better at SR = 1 at both axial locations. However, the calibration is less accurate when SR = 0 and 0.5, particularly at y = 7 mm. This suggests that the penumbra effect calibration performs well on larger EPL (EPL > 0.4 mm) but is not as accurate when dealing with smaller EPL (EPL < 0.4 mm). The penumbra has a large influence near the spray edges where the EPL is smaller and the signal-to-noise ratio is also small. The penumbra effect calibration also enhances the noise in this region.

According to Figures 9, 11 and 13, the EPL at y = 7 mm does not show a monotonic increasing or decreasing relationship with swirl ratio. When SR = 0, the maximum EPL is 0.27 mm (Figure 9). The maximum EPL decreases to 0.07 mm when swirl ratio increase to 0.5 (Figure 11). The maximum EPL increases to 0.6 mm when swirl ratio increases to 1 (Figure 13). The smaller EPL at the same vertical position suggests a higher atomization level at the same liquid and gas flow rate. This demonstrates that when the swirl ratio increased from 0 to 1, the atomization first increased and then decreased. When there was no swirl (SR = 0), only co-flow air stretched and broke the liquid phase in the axial direction, creating a slimmer spray. When swirl air was added, it helped to shear the liquid phase in the azimuthal direction as well, promoting the atomization process. However, when the swirl ratio was too high, it helps confine the spray, prevents its spread, and decreases the overall atomization. These results are supported by spray angle measurements in a companion paper [21].

Unlike the situations at y = 7 mm, Figures 8, 10 and 12 imply similar EPL distributions in both shape and range at y = 1 mm. The widths of the spray at y = 1 mm with different swirl ratios are all about 2-2.5 mm. The amplitudes of the plots in Figures 8, 10 and 12 are 2.3, 2.0 and 2.2, respectively. This is due to the liquid core at the position close to the nozzle exit. Here, the liquid jet has not completely broken up, forming a continuous liquid phase surrounded by droplets.

Conclusions

The current work compared the EPL of sprays from an airblast atomizer using narrowband synchrotron X-rays and broadband tube source X-rays. Data were presented at Re_l = 1,000 and Re_g = 16,700, with SR = 0, 0.5 and 1. Penumbra and beam hardening/ attenuation coefficient calibrations were applied in the broadband data with reasonable results. The penumbra effect calibration works better at large EPL than smaller EPL. At y = 7 mm below the nozzle exit, the relationship between swirl ratio and the EPL distribution suggests that swirl ratio and the atomization exhibits non-monotonic behaviour. Moreover, the liquid core was observed at y = 1 mm below the nozzle exit. In future work, additional flow conditions will by analysed.

Acknowledgements

This work was sponsored by the Office of Naval Research (ONR) as part of the Multidisciplinary University Research Initiatives (MURI) Program, under grant number N00014-16-1-2617. The views and conclusions contained herein are those of the authors only and should not be interpreted as representing those of ONR, the U.S. Navy or the U.S. Government.

This work was performed at the 7-BM beamline of the Advanced Photon Source, a U.S. Department of Energy (DOE) Office of Science User Facility operated for the DOE Office of Science by Argonne National Laboratory under Contract No. DE-AC02-06CH11357.

References

[1] Jiménez-Martín, E., Gharsallaoui, A., Pérez-Palacios, T., Carrascal, J. R., and Rojas, T. A., "Suitability of using monolayered and multilayered emulsions for microencapsulation of ω-3 fatty acids by spray drying: effect of storage at different temperatures," *Food and Bioprocess Technology*, 8(1): pp. 100-111, 2015.

[2] Sirignano, W. A., "Fuel droplet vaporization and spray combustion theory," *Progress in Energy and Combustion Science*, 9(4): pp. 291-322, 1983.

[3] Gomez, A., and Tang, K., "Charge and fission of droplets in electrostatic sprays," *Physics of Fluids*, 6(1): pp. 404-414, 1994.

[4] Som, S., and Aggarwal, S. K., "Effects of primary breakup modeling on spray and combustion characteristics of compression ignition engines," *Combustion and Flame*, 157(6): pp. 1179-1193, 2010.

[5] Linne, M., Paciaroni, M., Hall, T., and Parker, T., "Ballistic imaging of the near field in a diesel spray," *Experiments in Fluids*, 40(6): pp. 836-846, 2006.

[6] Berrocal, E., Kristensson, E., Richter, M., Linne, M., and Aldén, M., "Application of structured illumination for multiple scattering suppression in planar laser imaging of dense sprays," *Optics Express*, 16(22): pp. 17870-17881, 2008.

[7] Linne, M., "Imaging in the optically dense regions of a spray: A review of developing techniques," *Progress in Energy and Combustion Science*, 39(5): pp. 403-440, 2013.

[8] Heindel, T. J., "A review of X-ray flow visualization with applications to multiphase flows," *Journal of Fluids Engineering*, 133(7): pp. 074001, 2011.
[9] Kastengren, A., and Powell, C. F., "Synchrotron X-ray techniques for fluid dynamics," *Experiments in Fluids*, 55(3): pp. 1686, 2014.
[10] Kastengren, A. L., Powell, C. F., Wang, Y., Im, K. S., and Wang, J., "X-ray radiography measurements of diesel spray structure at engine-like ambient density," *Atomization and Sprays*, 19(11), 2009.
[11] Kastengren, A. L., Tilocco, F. Z., Duke, D., Powell, C. F., Zhang, X., and Moon, S., "Time-resolved X-ray radiography of sprays from engine combustion network spray a diesel injectors," *Atomization and Sprays*, 24(3), 2014.
[12] Li, D., Bothell, J. K., Morgan, T. B., Heindel, T. J., Aliseda, A., Machicoane, N., and Kastengren, A. L., "High-speed X-ray imaging of an airblast atomizer at the nozzle exit," *Gallery of Fluid Motion in APS-DFD 2017: 70th Annual Meeting of the APS Division of Fluid Dynamics*, Denver, CO - November 19-21, 2017, https://doi.org/10.1103/APS.DFD.2017.GFM.V0026 (accessed 03/23/2018).
[13] Heindel, T. J., Li, D., Morgan, T. B., Bothell, J. K., Aliseda, A., Machicoane, N., and Kastengren, A. L., "X-ray observations in the spray near-Field using synchrotron X-rays," in *ILASS-Americas: 29th Annual Conference on Liquid Atomization and Spray Systems*, Atlanta, GA, May 15-18, 2017.
[14] Brooks, R. A., and Di Chiro, G., "Beam hardening in X-ray reconstructive tomography," *Physics in Medicine & Biology*, 21(3): pp. 390, 1976.
[15] Halls, B. R., Heindel, T. J., Kastengren, A. L., and Meyer, T. R., "Evaluation of X-ray sources for quantitative two-and three-dimensional imaging of liquid mass distribution in atomizing sprays," *International Journal of Multiphase Flow*, 59: pp. 113-120, 2014.
[16] Machicoane, N. and Aliseda, A., "Experimental characterization of a canonical coaxial gas-liquid atomizer," in *ILASS - Americas 2017: 29th Annual Conference on Liquid Atomization and Spray Systems*, Atlanta, GA, May 15-18, 2017.
[17] Heindel, T. J., Gray, J. N., and Jensen, T. C., "An X-ray system for visualizing fluid flows," *Flow Measurement and Instrumentation*, 19(2): pp. 67-78, 2008.
[18] Kastengren, A., Powell, C. F., Arms, D., Dufresne, E. M., Gibson, H., and Wang, J., "The 7BM beamline at the APS: A facility for time-resolved fluid dynamics measurements," *Journal of Synchrotron Radiation*, 19(4): pp. 654-657, 2012.
[19] Dawson, D. J., Harper, J. M., and Akinradewo, A. C., "Analysis of physical parameters associated with the measurement of high-energy x-ray penumbra," *Medical Physics*, 11(4): pp. 491-497, 1984.
[20] Halls, B. R., Morgan, T. B., Heindel, T., Meyer, T. R., and Kastengren, A., "High-speed radiographic spray imaging with a broadband tube source," In *AIAA 2014: 52nd American Institute of Aerospace and Astronautics Aerospace Sciences Meeting*, National Harbor, MD, January 13-17, 2014.
[21] Bothell, J. K., Li, D., Morgan, T. B., Heindel, T. J., Aliseda, A., Machicoane, N., and Kastengren, A. L., "Characterizing the near-field region of a spray using white beam and focus beam X-ray measurements," in *ICLASS 2018: 14th Triennial International Conference on Liquid Atomization and Spray Systems*, Chicago, IL, July 22-26, 2018.